A microfluidic device for inferring metabolic landscapes in yeast monolayer colonies.

Running title : Emergence of metabolic landscapes in yeast monolayer colonies

Zoran S Marinkovic[1,2,3], Clément Vulin[1,4,5], Mislav Acman[1,3], Xiaohu Song[2], Jean Marc Di Meglio[1], Ariel B. Lindner[*,2,3], Pascal Hersen[*,1]

[1]*Laboratoire Matière et Systèmes Complexes, UMR 7057 CNRS & Université Paris Diderot, 10 rue Alice Domon et Léonie Duquet, 75013 Paris, France.*
[2]*U1001 INSERM, 24 Rue du Faubourg St Jacques, 75006, Paris, France.*
[3]*CRI, Université Paris Descartes, 8-10 Rue Charles V, 75004, Paris, France.*
[4]*Institute of Biogeochemistry and Pollutant Dynamics, ETH Zurich, Zurich, Switzerland.*
[5]*Department of Environmental Microbiology, Eawag, Dübendorf, Switzerland.*

**Correspondence and requests for materials should be addressed to Ariel Lindner (ariel.lindner@inserm.fr) or Pascal Hersen (pascal.hersen@univ-paris-diderot.fr).*

Keywords*:* Yeast colony, Microfluidics, Gene expression, Spatial Organization, Metabolism.

Abstract

Microbial colonies are fascinating structures in which growth and internal organization reflect complex morphogenetic processes. Here, we generated a microfluidics device with arrays of long monolayer yeast colonies to further global understanding of how intercellular metabolic interactions affect the internal structure of colonies within defined boundary conditions. We observed the emergence of stable glucose gradients using fluorescently labelled hexose transporters and quantified the spatial correlations with intra-colony growth rates and expression of other genes regulated by glucose availability. These landscapes depended on the external glucose concentration as well as secondary gradients, e.g., amino acid availability. This work demonstrates the regulatory genetic networks governing cellular physiological adaptation are the key to internal structuration of cellular assemblies. This approach could be used in the future to decipher the interplay between long-range metabolic interactions, cellular development and morphogenesis in more complex systems.

Introduction

Structured cellular communities are complex, dynamic systems and their composition, expansion and internal structure are the result of interactions between the cells and their microenvironment. Cells absorb and metabolize nutrients and also produce and secrete metabolites, creating spatial gradients of nutrients and metabolites. Thus, cells at the outskirts of a multicellular assembly do not experience the same microenvironment as the cells deeply buried within. Reciprocally, cellular physiology is dependent on the cell's position within a colony. Such variations in cellular physiology are consistently observed in a variety of multicellular systems – from bacterial and yeast colonies[1,2] to biofilms[3] and tumors[4,5] – and are reflected by altered gene expression levels and cellular phenotypes as growth rates, nutrient uptake rates and metabolic activity. Such variations presumably emerge because of long-range metabolic interactions between cells, in that the cellular microenvironment at one position depends on the nutrient uptake rate at another position.

Notably, multicellular communities[6–8] exhibit various adaptive benefits, including higher cell proliferation, improved access to resources and niches[9], collective defence (*e.g.*, against antagonists, drugs, antibiotics)[3] resulting in optimization of population survival when confronted with averse physical, chemical, nutritional or biological challenges[10]. These examples indicate the importance of understanding the emergence and maintenance of complex spatial multicellular structures from ecological[11–13], medical[14–16] and evolutionary[17–19] perspectives. Yet, despite the obvious contrast between homogeneous environments and the pronounced environmental heterogeneity of microbial cellular assemblies, the majority of scientific research to date has either focused on single cells in homogeneous environments or populations of cells grown in batch or continuous liquid cultures. This is mostly due to the complexity of designing an experiment that would allow monitoring, over long time, the development of a spatially defined extended multicellular assembly. This is in particular the case for the widely used eukaryotic model organism yeast *Saccharomyces cerevisiae*, despite the numerous calls in recent reviews to study its nutrient sensing, signalling, and related growth and development control within the natural colony context. [20–22].

57 As microorganisms in nature tend to live in multicellular communities, devising an experimental approach
58 that captures this complexity while being easy to use and amenable to different experimental needs and
59 conditions should further our understanding of complex gene regulatory networks in the context of
60 microbial evolution and ecology.
61
62 Current direct observations of three-dimensional colonies and biofilms are cumbersome and often
63 constrained by existing technologies[3]. For example, two-photon microscopy of sliced agarose-encapsulated
64 yeast colonies was required to show that yeast cells may adopt different physiologies – and possibly
65 different cell types – depending on their position within a colony[2]. In another example, nanospray
66 desorption electrospray ionization mass spectrometry (nanoDESI MS) was used to study growing bacterial
67 colonies on agar plates and showed a wide diversity and complexity of compounds that characterise
68 microbial chemical ecology[23,24]. Such complex methodologies are not amenable to time-lapse imaging, nor
69 to observation of the temporal variations in gene expression and growth rates of single cells over relevant
70 time and length scales. An alternative is to grow microbial cells in microfluidic devices to spatially constrain
71 the growth of the cells and to control the delivery of nutrients[25–29]. Microfluidic experimental research is
72 typically designed to ensure that the cells being studied experience a homogeneous environment. This can
73 be done at the single cell level, as it has been demonstrated in studies of aging of yeast[30] and bacteria[31]
74 where single cells had to be trapped and kept under constant nutrient flow for long term observations to
75 capture their death. Alternatively, a small cell assembly can be trapped in dead-end chambers under
76 assumption that a quick diffusion of nutrients will keep the environment in chambers homogeneous. With
77 that approach cell lineages were tracked for bacteria[32] (the widely used "mother machine") and yeast[33], cells
78 were subjected to fluctuating environments of different carbon sources to study non-genetic memory in
79 bacteria[34], and bacterial colonies were synchronised through quorum sensing and gas-phase redox
80 signalling over centimetre-length scales to produce oscillating colony "biopixels"[35]. Although fascinating
81 in their own right, unfortunately, such devices do not capture emerging properties at a colony level, *i.e.*
82 spatial variations in growth rates, microenvironments and phenotypes. Recently, there have been a few
83 attempts to use microfluidics to study collective properties of bacterial colonies grown in a microcolony.

84 Hornung *et al*. grew two-dimensional bacterial microcolonies in a 75 μm long device perfused with a very
85 low concentration (up to 195 μM) of protocatechuic acid as the only carbon source from both sides of the
86 cell chamber[36]. They observed heterogeneous growth which they confirmed through reaction-diffusion
87 model combined with particle-based simulations. In a similar setup, a 60 μm long device perfused with a
88 very low concentration of glucose (up to 800 μM) from one side was used to study the emergence of
89 microscale gradients that resulted in metabolic cross-feeding between glucose-fermenting and acetate-
90 respiring subpopulations of bacteria and antibiotic tolerance by slow growing subpopulation[37]. Wilmoth *et*
91 *al*. used microwells up to 100 μm in diameter to look at spatial patterns of H1-Type VI secretion system
92 (T6SS) mutants of *Pseudomonas aeruginosa* accompanied with an agent-based model depicting the two
93 observed subpopulations[38]. They found that spatial constraints and local concentrations of growth substrates
94 affect the spatial organization of cells. Finally, Liu *et al*. grew *Bacillus subtilis* biofilms perfused with
95 glycerol and glutamate media. They discovered collective oscillations which emerge as a consequence of
96 long-range metabolic co-dependence between cells in the interior and cells at the periphery of a biofilm,
97 presumably to maximize the availability of nutrients and survival of interior cells[39]. While the use of
98 microfluidics gave rise to the discovery of interesting collective properties of microbial assemblies, such
99 attempts were too specific and had to deal with some of the limitations like small device dimensions (<100
100 μm), use of low nutrient concentrations (<1 mM), limited scope of nutrient types, inability to access single
101 cell level – and therefore cannot be transposed to the general case of the study of a large monolayer of cells
102 in standard range and scope of nutrients employed in biological research. Additionally, it is tempting to
103 reconstruct the emergence of gene expression landscapes on a global scale (*e.g.,* within structured
104 communities) from local (*e.g.,* single cell) properties, given the extensive knowledge accumulated on
105 single-cell gene regulatory networks. However, the variations in the microenvironment within a
106 multicellular assembly and their interconnections with gene expression and cell metabolism are poorly
107 known.
108
109 In order to address the above limitations in current methodologies and observe emerging properties at a
110 colony level, we developed a microfluidic device to grow thin, extended arrays of yeast cell monolayers

111 that are perfused with nutrients from a single direction. We demonstrate a novel capacity to reproduce and
112 quantify spatial variation in cellular growth rate and the formation of gene expression landscapes for key
113 metabolic genes involved in glucose transport and utilization, across the nascent 2D microcolony.
114 Interestingly, the gene expression landscapes exhibited a high degree of spatial correlation over a range of
115 glucose concentrations. Notably, we show that an extended assembly of cells presents a spatial transition
116 between fermentative (high glucose environment, fast growth, rapid glucose utilization) and respiratory
117 (low glucose environment, slow growth, slow but efficient glucose utilization[40,41]) regimes, located close
118 to and far from the nutrient source, respectively. This spatial structure emerges from the interplay between
119 how cells individually adapt to the microenvironment and, at the same time, alter their surroundings as a
120 result of their metabolic activity. Said differently, cells collectively create, and experience, a spatially
121 structured micro-environment.
122

123 Results

124 **Growing extended yeast monolayers.** Microfluidic systems are usually designed to ensure a homogeneous
125 microenvironment for all cells[25]. In contrast, in this study, we designed a microfluidic device – dubbed the
126 "yeast machine" – to grow long, narrow yeast monolayers with the aim of observing the emergence of
127 nutrient gradients and spatial variations in cellular growth and gene expression landscapes. We used soft
128 lithography techniques to fabricate a multi-layered microfluidic device composed of a large channel (to
129 flow nutrients) and an array of perpendicular, extended (800 μm-long), narrow (50 μm-wide), flat (4.5 μm-
130 high) dead-end chambers in which yeast cells can grow as monolayers while the media is supplied by a
131 pressure pump-based system with flow control (Figure 1, Supplementary Figure 1). The length of the dead-
132 end chambers was optimized to induce significant variations in the nutrient concentrations within the
133 chambers due to cellular nutrient uptake. The chamber width was large enough to avoid jamming during
134 cell growth due to geometric constraints and small enough to avoid generation of complex, cell-
135 recirculating flows induced by cell growth[42]. The chamber height was comparable to – but slightly larger

136 than – the average size of a yeast cell, so the cells were vertically constrained to facilitate single-cell imaging
137 and time-lapse fluorescence microscopy (Supplementary Figure 2).
138
139 The cells were injected into the main channel of the "yeast machine" and then forced into the dead-end
140 chambers by centrifugation using a homemade 3D-printed holding device attached to a spin coater (see
141 Supplementary Figure 1c, d; Methods). The main channel was washed with yeast synthetic complete growth
142 medium to remove excess cells; cells that were trapped in the dead-end chambers by centrifugation were
143 not removed by the washing step. Nutrients were flowed through the main channel and could passively
144 diffuse into the array of dead-end chambers. The cells formed growing monolayers that extended from the
145 closed end of the chamber and collectively progressed towards the nutrient source (*i.e.* the open end of the
146 chamber) as the cells pushed each other while growing (Figure 2a, b; Supplementary Movie 1). Cells
147 eventually filled each chamber, forming an extended two-dimensional colony composed of about 2500 cells
148 (Figure 2b, Supplementary Figure 2), typically ~10 cells wide and ~200 cells long. Cells could be observed
149 locally at high magnification (100× objective), while the whole assembly could be seen at low
150 magnification (10× objective). We recorded the cellular expansion and subsequent internal dynamics of
151 these long monolayers, as well as the landscape of expression of key fluorescently tagged endogenous
152 genes, over time and over an almost 1000-fold range of glucose concentrations (from 0.01% to 8% *w/vol*).
153
154
155

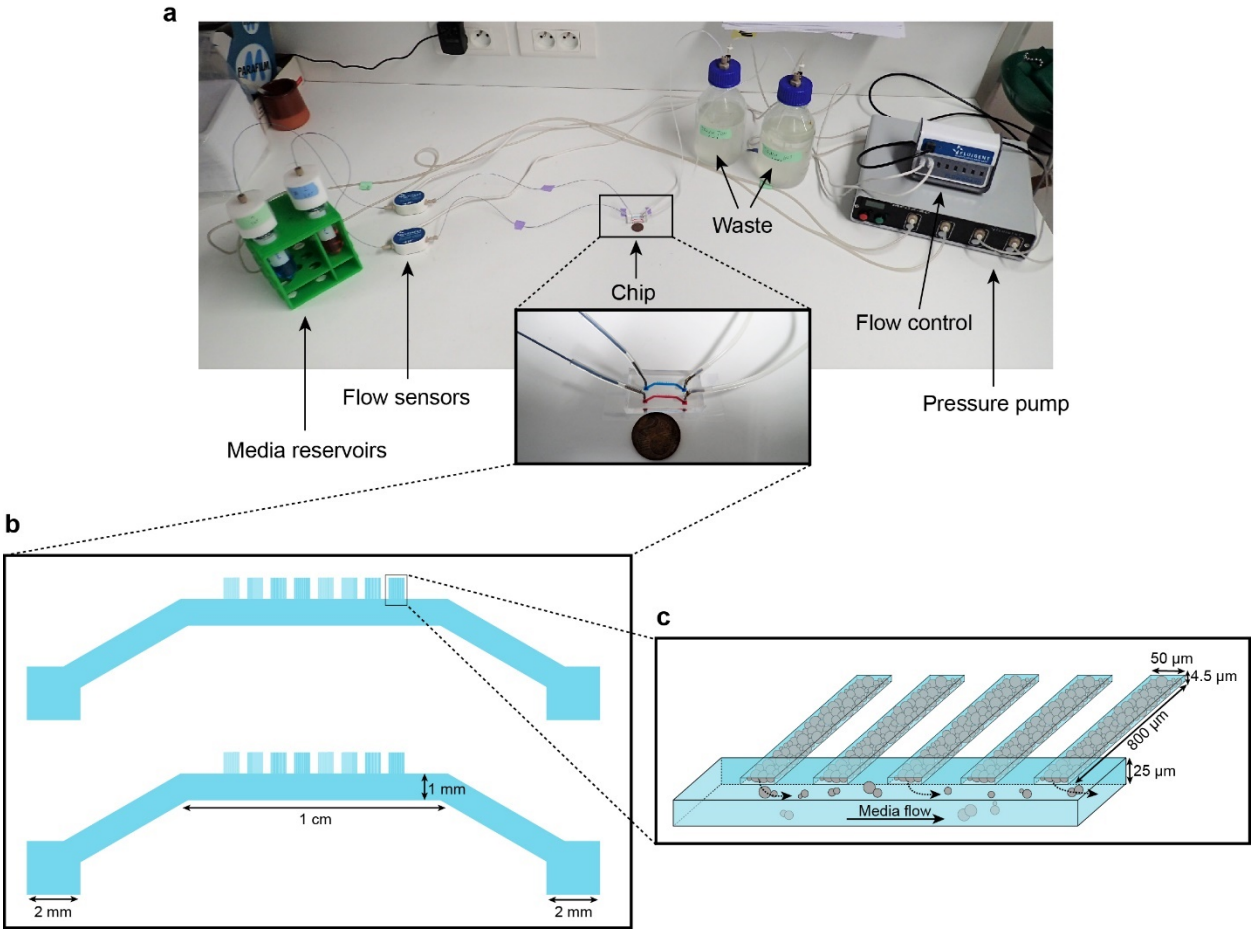

Figure 1. Microfluidic device setup and design. **1a**. Media reservoirs are pressurized with the help of Fluigent MFCS pressure pump resulting in flow through the flow sensors, into the chip and then to waste. Flow sensors and pressure pump are connected to the flow-rate control module, which maintains a constant flow through the system. Nutrient supply and media conditions can be changed in real time. **1b**. Each single "yeast machine" has two sets of cell chambers of various widths (5 µm, 10µm, 25 µm and 50 µm). The Cell chambers are connected perpendicularly to a large flow channel (1 mm wide, 25 µm high).. This design facilitates adaptation for different model systems (*e.g.* bacteria, yeast, mammalian cells) and high-throughput depending on the of predefined flexible length, width and height flexible adapted dimensions.. **1c**. A close-up sketch of a set of cell chambers used in our experiments. They are 800 µm long, 50 µm wide, and 4.5 µm high. A single cell chamber fits a monolayer of up to 2500 yeast cells. The whole setup is mounted on a microscope for time-lapse fluorescent imaging.

Monolayer in expansion displays regions of fast and slow growth. Expansion of the monolayers of cells was observed by microscopy at low magnification (10× objective). Under standard glucose-rich conditions (2*% w/vol*; 111 mM) and excess amino acids (5× CSM, see *Methods*), the front velocity, V_F, increased during the first 2-4 h and eventually reached a steady-state close to 100 µm.h^{-1} (Figure 2c, d, Supplementary Movie 1). Front velocity is the sum of the contribution of every cell to colony expansion. Therefore, V_F depends on the quantities of glucose and other nutrients that penetrate inside the yeast monolayer, which impact both the number of cells that grow and their growth rates. Initially, the monolayer is sparsely

175 populated and sufficient glucose is expected to reach all cells. After growth and division, a larger number
176 of cells can participate in global expansion of the population. Thus, the front velocity is expected to quickly
177 increase over time. However, at some point, as the size of the monolayer increases, the cells close to the
178 dead end of the chamber will stop growing (due to absorption and metabolism of available nutrients by
179 cells closer to the nutrient source/chamber opening) and the front velocity will plateau. Hence, after the cell
180 chamber populates with cells completely, a steady-state is reached where a constant number of cells with
181 access to glucose continue to divide and move passively towards the nutrient source, while the number of
182 cells at the dead end of the chamber deprived of glucose (and other nutrients) remains unchanged. If we
183 consider the ideal case in which yeast cells are 4 µm-wide and divide every 90 min in the presence of
184 glucose, each cell layer leads to an expansion of 4 µm every 90 min, or 2.6 $\mu m.hr^{-1}$. The observed terminal
185 front velocity of 94 ± 8 $\mu m.hr^{-1}$ (Figure 2) can be attributed to the first 36 ± 3 layers of cells, i.e. the first
186 140 µm of the colony. The glucose penetration distance can be approximated by assuming[1] that glucose –
187 of which the concentration is maintained at C_0 at the front of the monolayer – freely diffuses within the
188 assembly with a diffusion coefficient $D \sim 100\ \mu m^2.s^{-1}$ and is absorbed by cells at a constant rate, q_0, of ~ 1
189 $mM.s^{-1}$. Diffusion law dictates that the glucose concentration is expected to decrease significantly after a
190 typical distance, H, that scales with $\sqrt{\frac{DC_0}{q_0}} \sim 100\ \mu m$. Our direct observation (Figure 2e) showed that for a
191 layer of growing cells, H is around 400 µm at 2% *w/vol* glucose. Notably, both estimations are in agreement,
192 albeit they underestimate the observed size of the growing layer. These discrepancies result from discarding
193 the decay in the cellular growth rate at decreasing glucose concentrations and the variation in the specific
194 cellular uptake rate, q, with glucose concentration. Indeed, the interplay between glucose diffusion and
195 uptake is central to structuration of the colony as it affects both the number of cells that have access to
196 glucose and the glucose concentration in the microenvironment of each region, and thus determines which
197 cells actually participate in colony expansion and by how much[1]. The true glucose penetration distance is
198 therefore likely to be larger than the '*guesstimate'* above. Yet, inferring the true penetration distance would
199 require a detailed model of the dependency of both cellular glucose absorption and the growth rate on the
200 glucose concentration, as well as experimental measurements of the glucose concentrations within the
201 monolayer. This outlines the difficulty of predicting the internal structure of a simple yeast monolayer due

202 to our limited understanding of how yeast cells interact with nutrients and the difficulty of obtaining
203 quantitative details of the microenvironment landscapes within a yeast monolayer. In the following text,
204 we quantify the expression of different glucose concentration-dependent transporters as a possible proxy
205 for intra-colony glucose concentration. We even ventured further, to study how landscapes of cellular
206 growth and expression of key genes involved in glucose transport self-emerge from long-range metabolic
207 interactions within the yeast colony.
208
209 **Front velocity increases with glucose concentration.** Increasing the glucose concentration (from 0.01%
210 to 8% *w/vol*) led to higher terminal front velocities (Figure 2d), in agreement with the fact that at higher
211 concentrations, glucose will penetrate further by diffusion in the colony (Figure 2a). Thus, increasing the
212 concentration allows a larger number of cells to access glucose and participate in the growth of the colony.
213 Yet, the front velocity does not increase linearly with glucose concentration, and plateaus at very high
214 glucose concentrations (> 4% *w/vol*). One interpretation is that at this concentration range, sufficient
215 glucose reaches the dead end of the chamber, allowing all cells to participate in the growth of the assembly.
216 However, based on $V_F \sim \mu L$, where L is the length of the dead-end chamber and μ is the average cell growth
217 rate, one would expect a saturating front velocity of 368 $\mu m.h^{-1}$, much larger than the measured value of
218 100 $\mu m.h^{-1}$.
219
220 Glucose is not the only nutrient required for cellular growth; amino acids can be a limiting factor for
221 auxotrophic strains such as the one employed in this study (S288C background). This is why we used an
222 excess of amino acids (5× CSM) compared to classic SC medium for yeast cell cultures. Indeed, using
223 standard amino acid concentrations in the media resulted in significantly lower terminal front velocities,
224 even at high glucose concentrations (Supplementary Figure 3). This suggests that amino acid availability
225 can limit cellular growth, which is especially visible in the presence of high glucose concentrations, where
226 no longer glucose is limiting but rather amino acids are. As all experiments were performed under 5-fold
227 higher amino acid concentrations than normal SC medium, other metabolites that are consumed are likely
228 to form gradients within colony and might become rate-limiting for growth. Taken together, we conclude

229 that the spatial variations in all metabolic components of the microenvironment need to be taken into
230 account in order to fully understand microbial colony growth. With that in mind, building a mathematical
231 model to account for the observed expansion of a spatially structured colony is barely achievable, and we
232 will not address this question here. Rather, we opted to further characterize the development of glucose
233 gradients as a specific and critical component of the emergence of the metabolic landscape of the colony.
234
235 **Local expansion rate decreases with distance from the nutrient source.** Once the dead-end chambers
236 were filled with cells, we found the growth pattern was highly reproducible across parallel chambers at
237 each glucose concentration. The cells closer to the open end of the chambers continued to divide, pushing
238 cells out that were washed away by the flow in the nutrient channel. Cells closer to the dead end (y ~ 800
239 μm) did not move, grow nor divide. At standard glucose conditions (2% *w/vol*) and a high amino acid
240 concentration (5× CSM), significant cell motion was not observed after y ~ 400 μm, indicating that very
241 limited glucose is available to the cells that are beyond this region. By tracking single cell trajectories, we
242 measured the velocity field within the yeast monolayers over a range of glucose concentrations. We
243 extracted > 100 single cell trajectories per concentration, resulting in thousands of velocity data points (see
244 *Methods*). As expected, increasing the glucose concentration in the nutrient channel (from 0.01% to 8%
245 *w/vol*) led to higher local velocities deeper in the colony (Figure 2f, Supplementary Figure 4).
246 Concomitantly, velocity also increased closer to the chamber opening when cells experienced a higher
247 glucose concentration.
248
249 To sum up, our setup captures the essence of structured colonies, with the emergence of a landscape of
250 growth divided into a non-growing area and actively growing area. This spatial separation is the result of
251 the formation of glucose (and other nutrient) gradients. These gradients emerge as a result of cellular
252 metabolic activity, which in turn affects the cellular growth rate and physiology at the local scale.
253

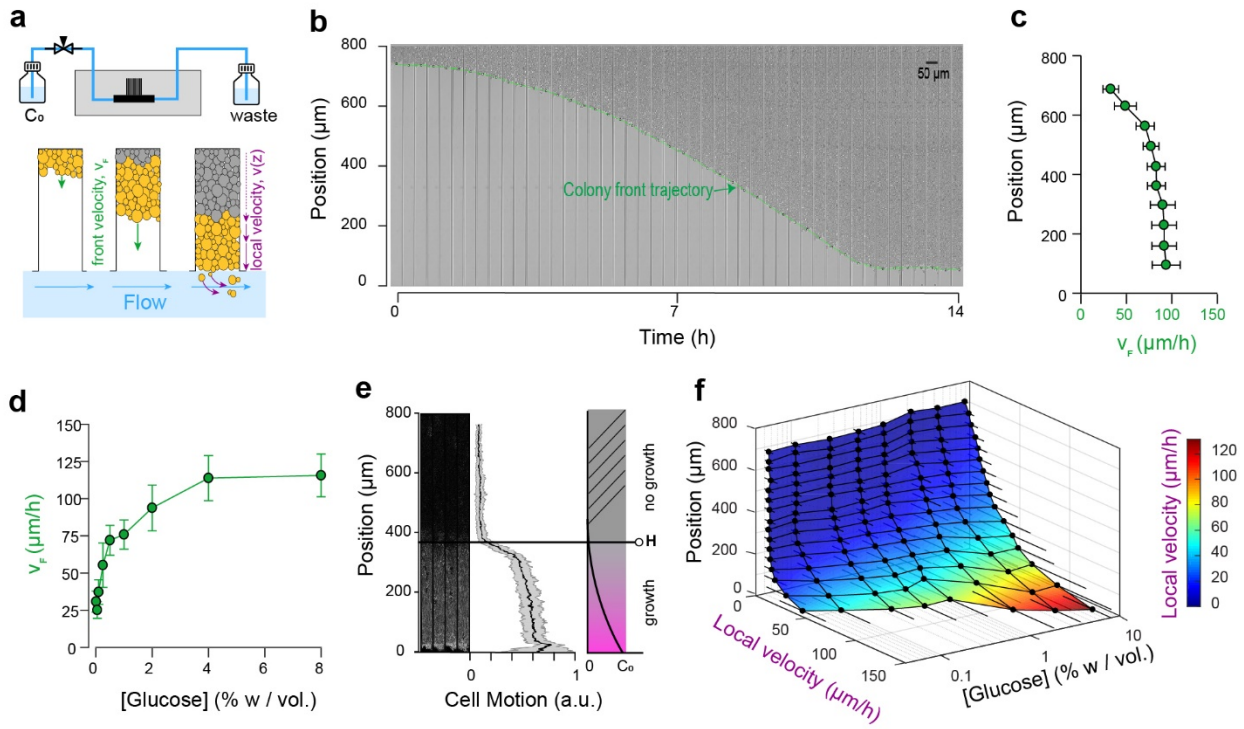

Figure 2. Expansion and dynamics of extended cellular monolayers. **2a.** The microfluidic device is perfused with nutrients using a pressure-driven system (see Figure 1). Yeast monolayers extend within the long chambers: front velocity (V_F) and local velocity (Vz) are determined by cellular growth and division. **2b.** Example of a time-lapse collage of yeast monolayer expansion along an 800 µm-long chamber (2% *w/vol*. glucose, 5× amino acid concentration). Front velocity increases and reaches a plateau (indicated by flattening of the slope of the green curve). When the front approaches close to the open end of the chamber (*i.e.,* 0 µm), the over-spilling cells are constantly washed away by the nutrient flow within the main channel. **2c.** Front velocity reaches a maximum when the position of the front becomes close to the open end of the chamber indicating that after expanding by a typical distance (~ 400 µm here for 2% *w/vol*. glucose), the maximal number of cells that receive glucose and can participate in expansion has been reached. 340 velocity data points binned into 10 equally spaced position points were extracted from n=12 colony front trajectories (2% *w/vol.* glucose). The error bars denote standard deviations of each bin (~15-30 velocity data points). **2d.** Front velocity as function of external glucose concentration. Data comes from the bin closest to the open end of the chamber as measured in Figure **2c** for each glucose concentration (n > 5). Error bars denote standard deviations. **2e.** Local cellular motion can be assessed by computing the standard deviation of pixel intensities across a stack of time-lapse images. Here, white areas indicate variations in movement across the time-lapse for cells below 400 µm, while the cells above do not move. Averaging over several channels (n=9), we obtained an indicator of cell motion and thus an estimate of the glucose penetration distance, *H* (~ 400 µm for 2% glucose). **2f**. Local velocity decreases for cells deeper within the chamber. Local velocity also increases with external glucose concentration. Velocity Data, that were binned into 16 equally spaced position, comes from the analysis of >100 cell trajectories. Error bars denote standard deviations.

Cellular metabolic activity creates gene expression landscapes. The emerging glucose (and other nutrient) gradients are expected to both trigger and be governed by differential gene expression landscapes. To this end, we studied the expression of seven key glucose transporters (HXT1-7) whose expressions are regulated by the extracellular glucose concentration. We employed yeast strains in which these endogenous glucose transporters were tagged with GFP (*Methods*), and recorded the fluorescence signals at the global scale using a low-magnification objective (10×) and local cellular scale using a high-magnification

261 objective (100×). Cells were loaded into the chambers as described above and observed after the
262 establishment of a quasi-steady state (starting 10 h after the chamber was filled with cells, Supplementary
263 Figure 5). We observed the formation of different landscapes of gene expression for each of the seven
264 transporters, each with marked territories of low and high expression (Figure 3, 4; Methods). In particular,
265 HXT1 and HXT7 displayed inversely correlated landscapes of gene expression (*e.g.*, Figure 3a, 3g for 2%
266 *w/vol* glucose). Both patterns demonstrate the formation and maintenance of a glucose gradient that emerges
267 from cellular metabolic activity. HXT1 is a low-affinity glucose transporter mainly expressed under high-
268 glucose conditions, while HXT7 is a high-affinity glucose transporter expressed under low-glucose
269 conditions only (Figure 3b, 3f)[43–45]. Concomitantly, HXT1 was expressed at the highest levels in the cells
270 close to the chamber opening (*i.e.,* in the highest glucose concentration), while HXT7 expression peaked
271 further away in the chamber, indicating a transition to a low-glucose region. We examined the cells at higher
272 magnification (60×) to assess the localisation of HXT7 gene expression. As expected, in the cells expressing
273 the highest levels of this gene, the fluorescence was localized to the cell membrane, indicating HTX7 played
274 an active role in glucose transport in these cells. In contrast, deeper in the colony, we observed lower levels
275 of HTX7 fluorescence due to the long lifetime of GFP-fused proteins and absence of dilution through cell
276 division, though this fluorescence was localized in vacuoles, indicating the transporter had been targeted
277 for degradation by the cells[46] (Figure 3a). Assuming the observed peak of HXT7 fluorescence matches the
278 peak fluorescence observed in batch culture at a glucose concentration of 0.016% *w/vol*. (Figure 3b, c,
279 Supplementary Figure 6), we could locate the position in the yeast monolayer at which the glucose
280 concentration reached 0.016% *w/vol*. This position was around $H_f \sim 500$ μm from the front, in good
281 agreement with the transition in cell motion (Figure 2, $H_m \sim 400$ μm).

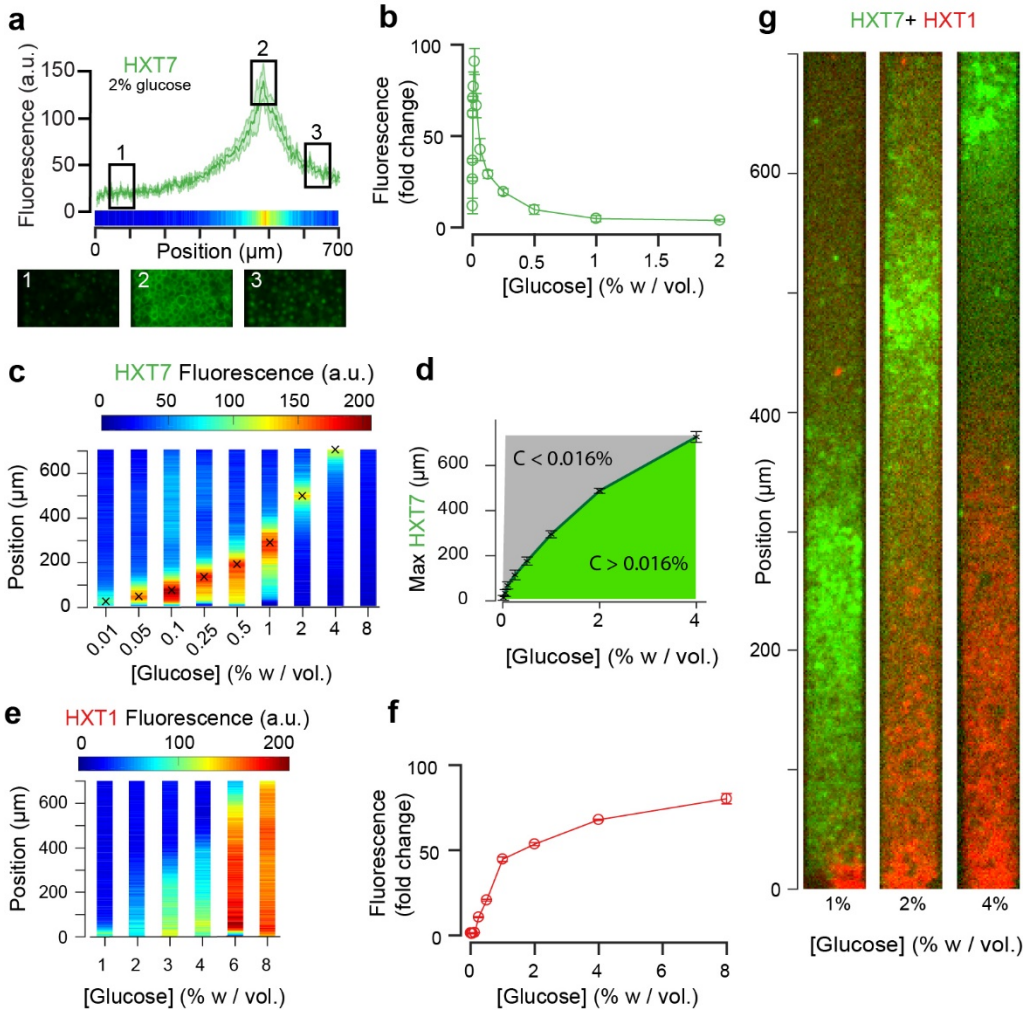

Figure 3. Landscapes of gene expression self-emerge in extended yeast monolayers. 3a. Expression profile of HXT7-GFP along the chamber (average fluorescence levels, n=9; standard deviation shown as the envelope) for an external concentration of 2% *w/vol* glucose. Membrane localization of HXT7 was only observed in the cells surrounding the area of peak HXT7 expression, localized at ~500 µm at 2% *w/vol*. glucose. **3b.** FACS measurements of HXT7-GFP expression in batch culture (average of three replicates) showing a single intensity peak at $C_0 = 0.016\%$. This peak value can be mapped back to the spatial landscape of **3a** to infer the glucose concentration in the region of peak HXT7-GFP fluorescence. n=3-6 per glucose concentration **3c.** On varying the glucose concentration in the nutrient channel, we observed a transition in peak HXT7-GFP fluorescence within the 2D colony. At a concentration of 4% *w/vol* and above, the peak was located close to the dead end of the chamber or not visible, indicating sufficient glucose was available throughout the chamber (color code normalized to maximal expression level). Data obtained from n=8-17 replicates per glucose concentrations (see also Supplementary Figure 6). **3d**. Compared with **3b,** it is possible to roughly define areas of glucose presence in the monolayer for a range of glucose concentrations (n=8-17, per glucose concentrations, error bars denote +/- one standard deviation). **3e**. Landscape of HXT1-GFP gene expression over a range of glucose concentrations (color code normalized to maximal expression); n=8-9 per glucose concentrations (see also Supplementary Figure 7). **3f.** FACS measurements of HXT1-GFP over a range of glucose concentrations; n=3 replicates. **3g**. Overlay of HXT1 (red) and HXT7 (green) gene expression landscapes at three external glucose concentrations, showing that the expression landscapes of these transporters were inversely correlated, in agreement with their different glucose-dependent expression patterns (compare **3b** and **3f**).

Gene expression landscapes depend on the glucose source concentration. Increasing the glucose concentration in the nutrient channel changed the gene expression landscape of all seven glucose

286 transporters (Figure 3, 4). In particular, at 1% *w/vol* glucose, HXT1 was only expressed at low levels at the
287 growing front of the colony ($y < 60$ μm). In contrast, at the highest glucose concentration (8% *w/vol*; Figure
288 3e, Supplementary Figure 7), HXT1 was expressed at high levels throughout the whole colony,
289 demonstrating glucose was available throughout the chamber. As HXT1 is mainly expressed under high-
290 glucose conditions (> 1% *w/vol* glucose) in batch culture[44], this observation indicated the glucose
291 penetration distance (within the chamber) increased with the external glucose concentration. This is in
292 agreement with the increase in local velocity with the external glucose concentration in Figure 2, with the
293 size of the growing area also increasing with the external glucose concentration.
294
295 In contrast, HXT7 exhibited a peak-like expression pattern, and was repressed under both high-glucose
296 conditions and when no glucose was present. At low-glucose concentrations (0.1% *w/vol*), a peak in HXT7
297 expression was observed at the very beginning of the colony ($y \sim 20$ μm), indicating glucose was quickly
298 absorbed by the cells closest to the chamber opening, thus these were the only cells with access to sufficient
299 carbon resources to grow and divide. The peak of HXT7 expression moved deeper into the colony as the
300 glucose concentration increased and disappeared completely at 8% *w/vol* glucose, again indicating
301 sufficient glucose could diffuse to the end of the chamber under high-glucose conditions (Figure 3, 4).
302
303 **Reconstructing glucose concentration landscapes using glucose transporter gene expression levels.**
304 We assessed the expression profiles of HXT1-7 in batch culture as a function of glucose concentration (see
305 *Methods*) to obtain a qualitative idea of the glucose concentrations within the microfluidic device. The data
306 for HXT7 was particularly revealing: its rather sharp, well-defined expression peak at 0.016% *w/vol*
307 allowed to define the distance in the microfluidic device at which the glucose concentration is close to that
308 value (Figure 3a, c). This concentration boundary separates the yeast monolayer into two regions with
309 different properties, *i.e.,* actively dividing and growth arrest. The position of this boundary moved deeper
310 into the colony as the external glucose concentration increased (Figure 3d).
311

312 We extended this idea further and used the complete HXT7 expression profile to infer the glucose
313 concentrations at all positions within the chambers. Assuming that the local level of HXT7
314 expression is only set by the local glucose concentration, we can use batch culture measurements
315 of HXT7 expression (based on flow cytometry) to determine the glucose concentration at a given
316 chamber position (Figure 4c, 4d). However, this only allows us to reconstruct the glucose
317 concentration gradient up to 0.016% *w/vol*., *i.e.* in the domain where cells are actively dividing.
318 The idea is simply to linearly map the two sets of measurements (in batch culture and in the
319 microfluidic device) based on the fluorescence levels that correspond to the maxima F_{max} and F'_{max}
320 and HXT7-GFP fluorescence levels at the chamber entry F_0 and F'_0. Using the data for HXT7 in
321 Figure 3, we were able to reconstruct the glucose gradient for different initial glucose
322 concentrations (Figure 4e). When applied to HXT1, the same inference led to very similar results
323 (Figure 4f). In both cases, glucose concentrations decay very quickly moving away from the
324 chamber opening and then exhibit a relatively long tail moving deeper into the colony.

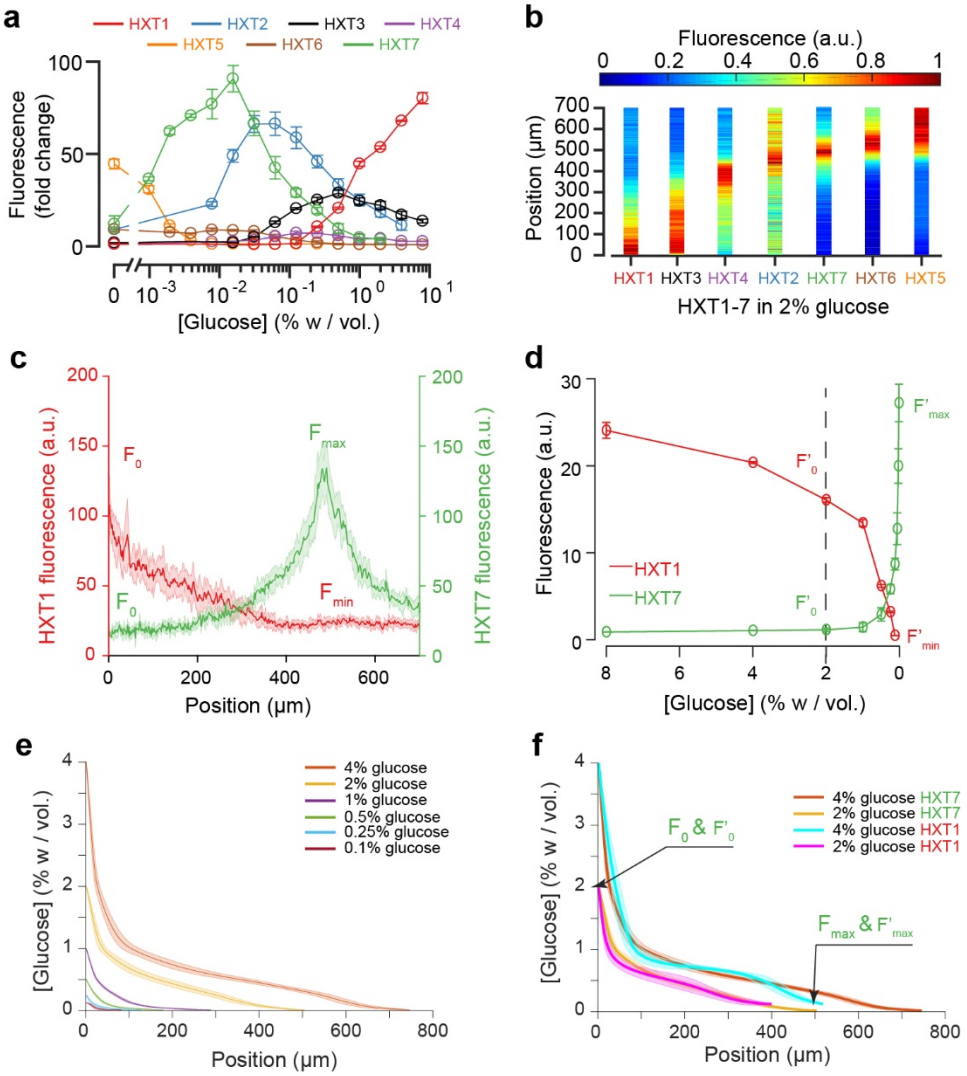

Figure 4. Using the fluorescence landscapes of glucose transporter gene expression to infer glucose concentration gradients. 4a. FACS measurements for HXT1-GFP to HXT7-GFP in batch culture over a range of glucose concentrations. The expression levels of each HXT show a specific dependence on glucose concentration (n=3-6 replicates per glucose concentration). **4b.** Landscapes of gene expression for all HXTs-GFP at an external glucose concentration of 2% *w/vol.* HXTs are ordered by their relative glucose specificity: HXT1 is expressed under high-glucose conditions, while HXT5 is only expressed at very low-glucose conditions. Assuming a progressive spatial decay in the glucose concentration away from the chamber opening, all maps of gene expression are in perfect agreement with the intensity profiles observed in batch culture (n=8-10 replicates per glucose concentration). **4c-d**. Method of glucose gradient reconstruction. The fluorescence landscape of HXT7 (*resp.* HXT1) shows a peak F_{max} (*resp.* a minimum, F_{min}) at a given location. The fluorescence intensity at the opening of the chamber, F_0, corresponds to the external glucose concentration, C_0. Using the FACS measurements of HXT7 (*resp.* HXT1) as a function of glucose concentration, one can define the concentration of glucose that matches the peak F_{max} (respective to the minimum F_{min}), and the fluorescence intensity that corresponds to C_0. This allows us to linearly map all other fluorescence intensities for a given glucose concentration from the batch culture to the fluorescence intensities inside the colony, allowing the glucose concentration across the entire cellular monolayer to be reconstructed. Data comes from previously mentioned HXT1 and HXT7 microfluidics and flow cytometry measurements. **4e-f.** Reconstruction of glucose concentration obtained from HXT7 (**4e, 4f**) and HXT1 (**4f**) fluorescence data and various external glucose concentrations.

Gene expression landscapes of other genes and transcription factor activity confirm the inferred glucose gradients. The fact the seven glucose transporters exhibited varied, robust spatial expression

327 patterns under identical conditions (*e.g.*, Figure 4a), together with the observed growth rate landscapes
328 (Figure 2), suggests cellular metabolic state varies significantly across the longitudinal axis of the yeast
329 monolayers. This variation was further assessed by mapping the expression and localisation of additional
330 key genes involved in glucose metabolism.
331
332 MIG1 is a key transcription factor involved in glucose repression that localizes to the nucleus in the
333 presence of glucose, to repress genes that participate in parallel carbon metabolic pathways (*e.g.,*
334 galactose)[20,21]. Observing the cells at high magnification, we quantified the distance after which MIG1
335 fluorescence was not present in the nucleus of the cells (Figure 5b, Supplementary Figure 8). This distance,
336 around 400 µm at C_0 = 2% *w/vol* glucose, was in excellent agreement with the data obtained by HXT7
337 profiling. Interestingly, the spatial transition from nuclear MIG1 to cytoplasmic MIG1 localisation was very
338 sharp and occurred over just a few cells.
339
340 In agreement with the batch culture observations, we found HXT5 was only expressed in regions with very
341 low or no glucose concentrations where the cells did not seem to divide over several hours (Figure 5a).
342 Therefore, HXT5 appears to be an excellent marker of growth arrest in this context[47].

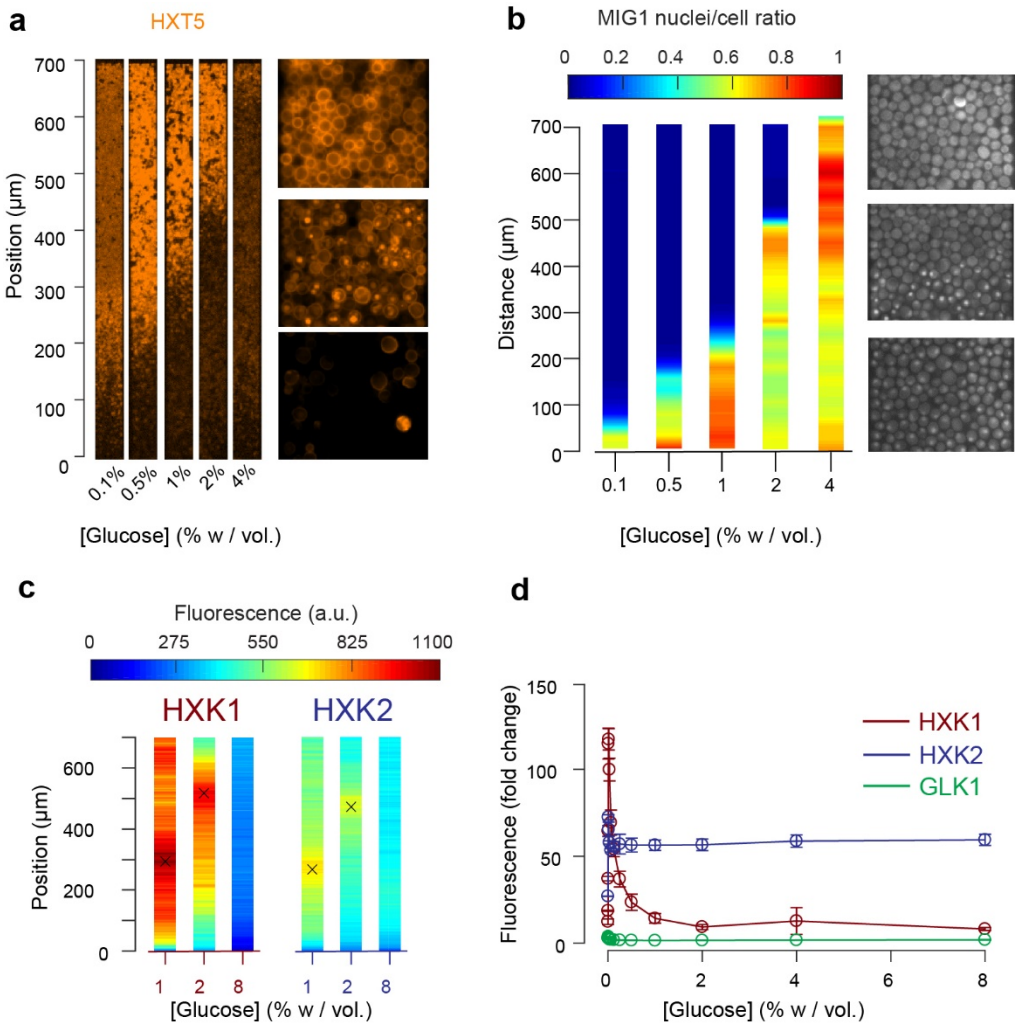

Figure 5: Other landscapes of genes involved in glucose metabolism. 5a. Landscape of HXT5 expression. HXT5 is expressed under very low and no glucose conditions and appears to be a good marker of growth arrest. At C_0 = 2% *w/vol*, HXT5 expression is in good agreement with the observed absence of cellular division (see Figure 2, Supplementary Figure 9). **5b.** Landscape of MIG1 activity. MIG1 fluorescence was located in the nucleus in the presence of glucose, with a sharp transition in nuclear localization observed (middle picture, at 2% *w/vol* glucose in the nutrient channel), confirming the existence of a glucose gradient (n=3 replicates). Total number of cells and cells with nuclear localization of fluorescence were annotated manually and binned into 25 µm bins (see also Supplementary Figure 8). **5c.** HXK1 and HXK2 are hexokinases involved in glucose metabolism. Their landscape of expression exhibited peaks that indicate a transition from high to very low glucose levels (n=8-9 replicates per glucose concentration). **5d.** FACS measurements of HXK1 and HXK2 expression over a range of glucose concentrations (n=3-6 replicates per glucose concentration).

The expression landscapes of two hexokinases involved in glucose metabolism, HXK1 and HXK2 (Figure 5c) that are expressed when cells are grown on non-glucose carbon sources, were also consistent with the batch measurements (Figure 5d, Supplementary Figure 11) and further validated the existence of a glucose gradient. For each profile, we extracted the position of maximal expression and inferred the glucose concentration at this position from the FACS measurements of batch cultures. The batch measurements indicated maximal HXK1 and HXK2 expression were observed at a glucose concentration of about 0.016%

350 *w/vol.* As expected, neither enzyme was expressed at very high glucose concentrations. The HXK1 and
351 HXK2 expression maxima were similar at the two other glucose concentrations studied, around 300 µm at
352 C_0 = 1% and 500 µm at 2% *w/vol*. Again, these data are in very good agreement with the positions of HXT7
353 peak expression at the same glucose concentrations.
354
355 Finally, we examined the expression of PDC1 and SDH2, which are overexpressed in fermenting and
356 respiring cells, respectively[48–50]. Their expression landscapes were inversely correlated (Figure 6a,
357 Supplementary Figure 10), indicating a transition from fermentative metabolic activity at the nutrient front
358 of the colony to respiratory metabolic activity towards the dead end of the chamber where glucose is scarce.
359 These expression maps are in good accordance with our previous results (Figure 2, 3, 5) and the levels of
360 PDC1 and SDH2 expression in batch culture (Figure 6b, 6c).

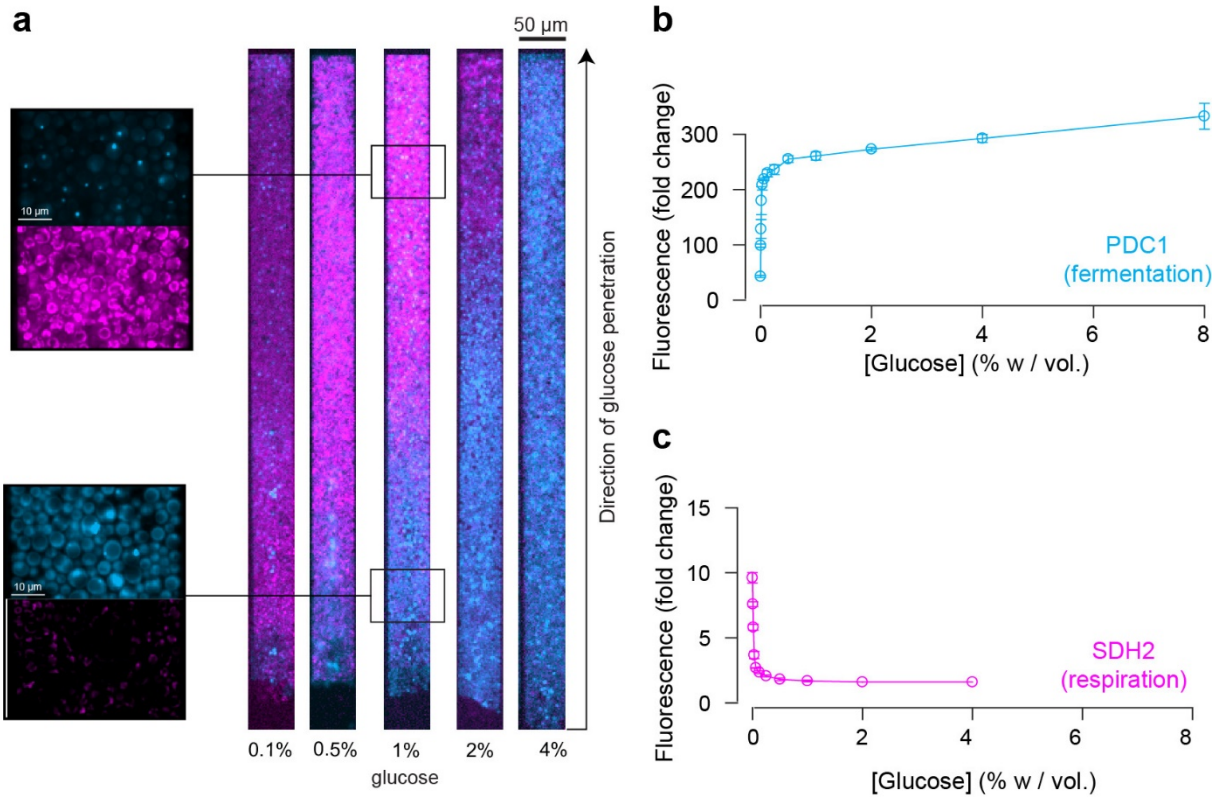

361

Figure 6. Impact of the glucose gradient on yeast physiology and the emergence of a landscape of phenotypes. 6a. Overlay of the landscapes of gene expression of PDC1 (blue) and SHD2 (pink). PDC1 is known to be expressed when yeast cells ferment, SDH2 is mainly expressed in respiring cells (see also Supplementary Figure 10). **6b.** FACS measurements of PDC1 expression over a range of glucose concentrations in batch culture (n=3). **6c.** FACS measurements of SDH2 expression over a range of glucose concentrations in batch culture. The inverse correlation between PDC1 and SDH2 expression observed in batch culture is in good agreement with the inversely correlated spatial expression patterns within yeast cell monolayers (n=3).

362 **Multiple gene expression landscapes are spatially correlated.** We decided to compare the landscapes of
363 gene expression for the entire set of reporter genes by aligning the different landscapes across varied
364 nutrient conditions (Figure 7a). Strikingly, all landscapes showed a high level of spatial correlation. Two
365 major landscapes emerged: peaking (*e.g.*, HXT7) and switching (*e.g.,* HXT1 or MIG1). We defined and
366 extracted the typical lengths of the peaking and switching landscapes (Figure 7b) and plotted them as
367 function of the external glucose concentration (Figure 7c). The typical lengths of all of these landscapes for
368 different reporter genes were remarkably close, despite the fact that we looked at different cellular
369 components: a transcription factor (MIG1), glucose transporters (HXTs), metabolic enzymes (HXKs) and
370 metabolic state reporters (SDH2, PDC1). Notably, we gained a global view of gene expression landscapes
371 and their interrelationships along a monolayer colony. All data showed the colonies were structured into
372 two regions with very different properties (Figure 7d): an actively growing region, where cells divide
373 abundantly and ferment glucose, and a quiescent area, where cells do not divide much and have switched
374 to respiratory metabolism to compensate for the very low glucose availability. While it is not surprising to
375 see the expression levels of metabolic genes vary with the glucose concentration, our approach
376 demonstrates genetic programs not only allow individual cells to adapt to changes in the nutrient
377 environment, but also enable multicellular assemblies to self-organize spatially through long-range
378 metabolic interactions. This sheds new light on the coordinated actions of these genes in a biologically
379 relevant multicellular context that has impact on ecology, evolution, development and emergence of
380 multicellularity.
381
382 **Overall, we studied how cells within a monolayer colony collectively shape their microenvironment**
383 **through long-range metabolic interactions. This is a complex process, in which cells adapt locally,**
384 **and shape a spatial landscape of gene expression as a global phenotype. As a whole, the structure of**
385 **an assembly of cells and the microenvironment landscapes emerge as the result of local cellular**
386 **metabolic activity.**
387

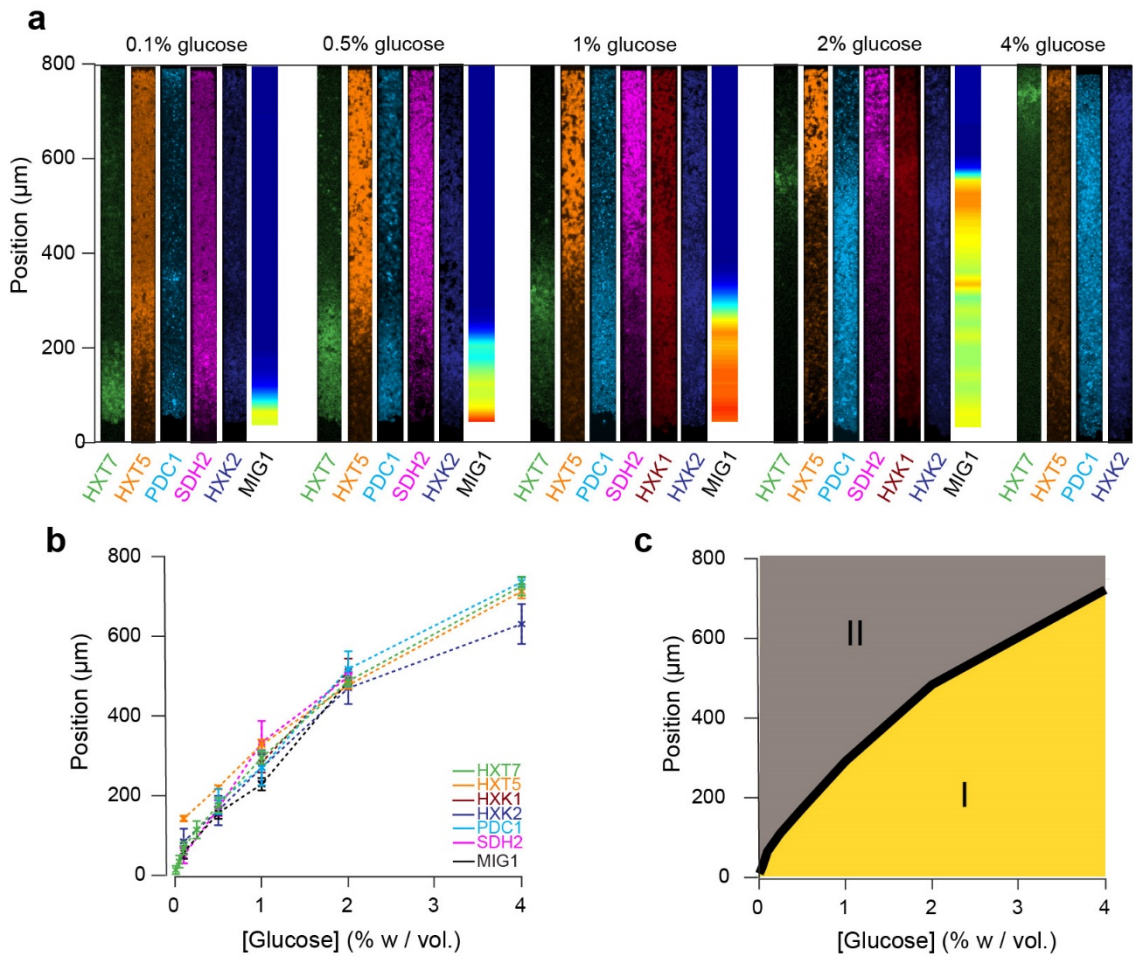

Figure 7: Global view of the emergence of landscapes of gene expression. 7a. The different landscapes of gene expression presented in this study are aligned, regrouped and displayed over a range of glucose concentrations. This simple view sheds light on the macroscopic spatial correlations between these different landscapes, which are both setting and traces of the establishment of glucose gradients. **7b.** For each gene expression landscape, we identified the fluorescence peak (HXT7, HXK1, HXK2) or the position of the transition between low and high expression (HXT1, HXT5, SDH2, PDC1) or activity of the transcription factor (MIG1). **7c.** Landscapes of gene expression delimit two regions in which cells are physiologically different. Phase I indicates active growth by fermentation in the presence of glucose; Phase II indicates growth arrest or very limited growth via respiratory metabolism at zero or close to zero glucose concentrations. The transition between the two phases typically takes place relatively sharply, over a hundred micrometers or ~ 20 cells.

Discussion

Here, we took an alternative point of view compared to traditional systems and single-cell biology. Rather than studying single-cell metabolic properties in a well-mixed, homogeneous environment, we designed a microfluidic chip to force yeast cells to grow and shape their microenvironment, solely by fixing the properties of the microenvironment at the boundary of the monolayer. This approach allowed us to measure simultaneously properties at both the single-cell scale and structured population scale and holds potential for establishing a quantitative link between these scales.

396

397 Specifically, we showed that cells self-generate nutrient landscapes that in turn influence cellular
398 metabolism and gene expression profiles. This behaviour, based on nutrient uptake adaptation, is generic
399 and feeds back on the behaviour of other cells through what we call non-specific long-range metabolic
400 interactions. Indeed, the microenvironment sensed by cells a few hundred micrometres inside a colony is
401 very different from the microenvironment experienced by the cells at periphery. Notably, gradients emerge
402 over relatively short distances, and this process may possibly affect studies of cellular populations within
403 microfluidics settings. More importantly, quantitative description of gene expression landscapes is critical
404 if one wants to understand the establishment and behaviour of cellular communities, whether these are as
405 simple as yeast colonies or more complex, such as biofilms and complex microbial ecosystems in which
406 several types of cells cohabit and interact. Indeed, in addition to the described long-range metabolic
407 interactions, many other environmental and genetic determinants such as intercellular communication, cell
408 surface properties, cell-cell adhesion strength and secretion of extracellular matrix components have been
409 shown to participate in the emergence of the complex morphology[3,51,52] and internal structure of microbial
410 colonies in such complex situations. The nature of many of these interactions could also be studied using
411 similar microfluidic devices to identify the relative contribution and relationship of environmental and
412 genetic determinants to the metabolically generated microenvironment.

413

414 We have made significant advances in the study of emerging properties of yeast colony growth,
415 microenvironment formation and gene expression compared to previously published studies [2,53,54]. These
416 studies have shown fascinating differentiation and diversity within yeast colonies grown on agar but their
417 relevance to study the dynamical emergence of complexity in microbial colonies is limited by their
418 methodology (*e.g.*, growth on a single specific medium with no dynamic control of environmental changes,
419 two-photon microscopy, unsuitable for live time-lapse microscopy, obligation to section colonies *etc.*)
420 which does not allow detailed spatiotemporal analysis of cellular growth, microenvironment and gene
421 expression landscapes at a relevant single-cell scale. Our approach is designed to access the dynamics of
422 large microbial colonies, and while we did not report it here, it is straightforward with microfluidics to

423 dynamically change in frequency and composition the external environment, and as such to analyse how
424 colonies adapt their internal organisation to such stresses.
425
426 Our results are in most part in line with the knowledge of glucose metabolism obtained in batch culture.
427 Yet, our methodology sheds quantitative description of the spatial expression of genes involved in the
428 glucose metabolism and its correlation with the cell local growth rates. Our results show that even in the
429 simple context studied here, reconstructing the microenvironment spatial structure from single-cell
430 measurement is not trivial. A proper model should take into account how the growth rate and specific
431 absorption rate vary with the glucose concentration and the microenvironment. Modelling the entire
432 complexity of the microenvironment is hardly possible, even with today's knowledge. Thus, we decided to
433 take a different approach and use key genes involved in glucose metabolism to infer the glucose
434 concentration gradient. We showed that different reporter genes consistently reported the same glucose
435 gradient. We envision that the data extracted from relevant fluorescent reporters could be fed into an agent-
436 based or mean-field models that take cell-cell interactions, mechanics and spatial diffusion of metabolites
437 into account to fill the gap between data generated from single cells to data that is relevant to evolution and
438 ecology, *i.e*. at the colony scale. We anticipate that linking local properties to macroscopic, global behaviour
439 will help to understand the architecture of microbial communities and how evolution shapes the
440 development of these architectures through long-range metabolic interactions. Of note, in another rare
441 attempt to study emergence of population level phenomena in yeast *S. cerevisiae* Campbell *et al*. looked
442 at the synthetic "self-establishing communities" that were able to cooperatively exchange metabolites[55].
443 They inoculated on agar plate auxotrophic *S. cerevisiae* strain that had different auxotrophic markers on
444 plasmids. As cells were dividing, some of the plasmids that complemented yeast auxotrophy and therefore
445 rescued their growth were lost, resulting in a colony which is composed of yeast that are auxotrophic for a
446 certain amino acid. However, they were able to grow because they used amino acids that were released in
447 the environment by other yeast that were producing it, effectively generating a very heterogeneous colony
448 that sustained growth through metabolite exchange. Interestingly, previous efforts to co-culture
449 complementary auxotrophs had limited effectiveness in supporting co-growth in liquid cultures, indicating

450 the importance of spatial structure in facilitating cooperation and makes our system very attractive for study
451 of such phenomena[56].
452
453 Furthermore, while the spatial microenvironment is not fully characterized, we have shown that the
454 emergence of gradients, and simultaneously gene expression landscapes, are robust and reproducible
455 features of the colony. Moreover, the landscapes can be compared to extract correlation patterns and infer
456 how gene regulatory networks act in synchronicity to establish the microenvironment within the colony.
457 This approach may provide a relatively simple, yet effective method of screening for "organismic"
458 properties that have been shaped by evolution and are only relevant in a multicellular context.
459
460 Our future efforts to extend the application of this setup will be dedicated to the study of how the
461 microenvironment dynamically changes when external conditions are altered, an uncharted territory at the
462 scale of a multicellular assembly that is central to the understanding of microbial ecosystem resistance to
463 stress, environmental fluctuations and adaptation. **We anticipate that similar approaches could be used**
464 **to study aging, cooperation and competition, cell memory or evolutionary dynamics, as well as**
465 **quantitative characterization of (synthetic) ecological systems and mixtures of cells relevant to**
466 **ecology and chemical biology.**
467

468 # Materials and Methods

469 **Yeast strains**. All experiments were performed using haploid *S. cerevisiae* strains derived from the S288C
470 background - BY4741: *MAT*a *his3Δ1 leu2Δ0 met15Δ0 ura3Δ0*. See Supplementary Table **T1** for a detailed
471 list of the yeast strains used in this study.
472
473 **Microscopy**. We used an inverted fluorescence microscope (IX81, Olympus) equipped with an EMCCD
474 camera (Evolve 512, Photometrics) and X-Cite exacte fluorescence light source (Lumen Dynamics).
475 Optical filters from Chroma Technology Corporation ET-EGFP (U-N49002; Ex 470/40nm Di495 Em
476 525/50nm) and ET-DsRed (U-N49005; Ex 545/30nm Di570 Em620/60nm) were used to observe GFP and

477 RFP fluorescence. Cells were observed using Olympus 10× (Plan 10x / 0.25 NA), 60× (PlanApo N 60x /
478 1.42 NA Oil) and 100× (UPlanFL N 100x / 1.3 NA Oil) objectives. Open-source µManager[57] microscopy
479 software was used to control all of these components and setup multi-dimensional acquisition. The
480 temperature inside the microscope incubation chamber that contained the media and cells was maintained
481 at 30 °C (Life Imaging Services). Fluorescence intensity was set to 10% of maximum output, fluorescence
482 exposure was set to 1000 ms and camera gain was set at maximum. The time interval between each
483 acquisition cycle was 6 min.
484
485 **Microfluidics and cell loading**. Microfluidic devices were constructed using soft lithography techniques.
486 Photomasks were drawn using L-Edit software (Tanner) and printed on a high-resolution glass substrate
487 (Delta Mask). A master wafer was created using SU-8 2000 (MicroChem) epoxy-based photoresist that
488 was spin-coated to the appropriate thickness and exposed to UV light using an appropriate photomask to
489 create the desired pattern. Multi-layered patterns were aligned and exposed to UV light using a MJB4
490 manual mask aligner (SUSS MicroTec) and the dimensions of the master wafer were checked using a
491 Dektak 150 surface profiler (Veeco). The master wafer was treated with 95% (3-mercaptopropyl)-
492 trimethoxysilane (Sigma) for 1 h in the vapour phase. Microfluidic chips were created by casting a degassed
493 10:1 mix of polydimethylsiloxane (PDMS) and curing agent (Sylgard 184 kit; Dow Corning) on the master
494 wafer, followed by at least 2 h curing at 65 °C. Each chip was gently cut and peeled off the master wafer;
495 the entry/exit ports were punched out. The chip and a glass coverslip (24 x 50 mm #1; Menzel-Gläser) were
496 treated with O_2 plasma for 1 min in a plasma cleaner (Harrick Plasma), bonded together and incubated at
497 65 °C for 10 min. Before loading cells, the chips were coated with 1% Pluronic F-127 (Sigma) for 30 min.
498 Cells were precultured overnight in 5 mL of synthetic complete (SC) medium containing 2% *w/vol* glucose
499 in a shaking incubator at 30 °C, diluted 50-fold into 50 mL of SC + 2% *w/vol* glucose, cultured for 5-6 h in
500 a shaking incubator at 30 °C to an OD_{600} of 0.2-0.4, collected by centrifugation, and loaded into the
501 microfluidic system with a pipette. The microfluidic system was centrifuged for 2 min at 1000 rpm using
502 3D-printed adaptors (Laurell WS-650 spin coater) to force the cells into the dead-end cell chambers. Liquid
503 media was flowed rapidly through the flow channel to remove excess cells and the flow rate was set to 5

504 μL/min. A pressure-based microfluidic flow control system (MFCS; Fluigent) coupled with a flow rate
505 platform (Fluigent) and a flow rate control module (Fluigent) that measured the flow rate and kept it
506 constant by adjusting the pressure through a feedback loop was used to push liquid media through the flow
507 channel. The output was kept at a constant pressure of 100 mbar above atmospheric pressure to minimize
508 formation of air bubbles inside the flow channel.
509
510 **Flow cytometry**. Flow cytometry experiments were performed on a Gallios Flow Cytometer (Beckman
511 Coulter) using a 488 nm excitation laser and 530/30 nm FL1 emission filter to detect GFP fluorescence.
512 Data analysis was performed using Kaluza Flow Cytometry Analysis Software (Beckman Coulter).
513 Approximately 10^4 cells were inoculated in 10 mL of SC medium containing various glucose concentrations
514 ($\log_2$ dilutions from 8% to 0.0078125%, and 0% *w/vol* glucose) and cultured in a shaking incubator at 30
515 °C to an OD_{600} of ~0.02-0.2 depending on the starting glucose concentration. Cells were then diluted 10-fold
516 into 10 mL of fresh SC media containing the same starting glucose concentration and grown for 4-5 h in a
517 shaking incubator at 30 °C, centrifuged at 4000 rpm for 10 min, re-suspended in 300 μL of PBS pH 7.4
518 buffer (Gibco) and fluorescence was measured using the flow cytometer. The supernatant of each sample
519 was collected, and the glucose concentration was measured using the Glucose (HK) Assay Kit (Sigma) to
520 confirm that the glucose concentration remained constant during the growth phase (Supplementary Figure
521 11a).
522
523 **Image analysis**. Image analysis was performed using open-source ImageJ 1.51p software[58]. To obtain front
524 velocity, we applied a threshold (Otsu) to detect the bottom frontier over time after flattening the
525 background using a FFT band-pass filter. The image signal is decomposed by FFT into a spectrum of its
526 constituent frequencies. Because some operations can be more easily performed on the spectrum than on
527 the original image, the FFT bandpass algorithm filters out large structures (shading correction) and small
528 structures (smoothing) of the specified size by gaussian filtering in Fourier space. The default parameters
529 are set at 40 pixels for large structure and 5 pixels for small ones. To compute the local speed of the cells
530 inside the cell assembly, we used the plugin TrackMate[59] v3.5.1 to track cell trajectories. TrackMate was

set to DoG detector with estimated blob diameter of 4 µm and threshold of 4, while tacking was set to linear motion LAP.

Acknowledgments

The authors would like to thank Sébastien Léon (IJM, CNRS) and their respective team members for their critical reading of this manuscript. This work was supported by the *Agence Nationale de la Recherche* (ICEBERG-ANR-10-BINF-06-01; ANR-16-CE12-0025-01), the interdisciplinary program of the *University Sorbonne Paris Cité*, the *Who am I?* Laboratory of Excellence (ANR-11-LABX-0071 and ANR-11-IDEX-0005-01) and the European Research Council (ERC) under the European Union's Horizon 2020 research and innovation programme (grant agreement No 724813).

Author Contributions

ZSM performed all experiments; ZSM, MA, ABL, PH analysed the data; ZSM, XS performed image analysis; ZSM, ABL, PH designed the experiments and wrote the manuscript with contributions from CV and JMdM.

Supplementary Information

Supplementary information contains eleven figures, one supplementary table and one supplementary movie.

References

1. Vulin, C. *et al.* Growing Yeast into Cylindrical Colonies. *Biophys. J.* **106**, 2214–2221 (2014).
2. Čáp, M., Štěpánek, L., Harant, K., Váchová, L. & Palková, Z. Cell Differentiation within a Yeast Colony: Metabolic and Regulatory Parallels with a Tumor-Affected Organism. *Mol. Cell* **46**, 436–448 (2012).

553 3. Nadell, C. D., Drescher, K. & Foster, K. R. Spatial structure, cooperation and competition in
554 biofilms. *Nat. Rev. Microbiol.* **14**, 589–600 (2016).
555 4. Carmona-Fontaine, C. *et al.* Emergence of spatial structure in the tumor microenvironment
556 due to the Warburg effect. *Proc. Natl. Acad. Sci.* **110**, 19402–19407 (2013).
557 5. Delarue, M. *et al.* Compressive Stress Inhibits Proliferation in Tumor Spheroids through a
558 Volume Limitation. *Biophys. J.* **107**, 1821–1828 (2014).
559 6. Shapiro, J. A. Thinking about bacterial populations as multicellular organisms. *Annu. Rev.*
560 *Microbiol.* **52**, 81–104 (1998).
561 7. Shou, W., Ram, S. & Vilar, J. M. G. Synthetic cooperation in engineered yeast populations.
562 *Proc. Natl. Acad. Sci. U. S. A.* **104**, 1877–1882 (2007).
563 8. Xavier, J. B. & Foster, K. R. Cooperation and conflict in microbial biofilms. *Proc. Natl. Acad.*
564 *Sci.* **104**, 876–881 (2007).
565 9. H. Koschwanez, J., R. Foster, K. & W. Murray, A. Sucrose Utilization in Budding Yeast as a
566 Model for the Origin of Undifferentiated Multicellularity. *PLoS Biol.* **9**, e1001122 (2011).
567 10. Palková, Z. & Váchová, L. Life within a community: benefit to yeast long-term survival.
568 *FEMS Microbiol. Rev.* **30**, 806–824 (2006).
569 11. Antwis, R. E. *et al.* Fifty important research questions in microbial ecology. *FEMS Microbiol.*
570 *Ecol.* **93**, (2017).
571 12. Gonzalez, A. *et al.* Characterizing microbial communities through space and time. *Curr. Opin.*
572 *Biotechnol.* **23**, 431–436 (2012).
573 13. Widder, S. *et al.* Challenges in microbial ecology: building predictive understanding of
574 community function and dynamics. *ISME J.* **10**, 2557–2568 (2016).
575 14. Bryers, J. D. Medical Biofilms. *Biotechnol. Bioeng.* **100**, 1–18 (2008).
576 15. Gilbert, J. A. *et al.* Current understanding of the human microbiome. *Nat. Med.* **24**, 392–400
577 (2018).

578 16. Estrela, S. & Brown, S. P. Community interactions and spatial structure shape selection on
579 antibiotic resistant lineages. *PLOS Comput. Biol.* **14**, e1006179 (2018).
580 17. Ratcliff, W. C., Denison, R. F., Borrello, M. & Travisano, M. Experimental evolution of
581 multicellularity. *Proc. Natl. Acad. Sci. U. S. A.* **109**, 1595–600 (2012).
582 18. Nadell, C. D., Foster, K. R. & Xavier, J. B. Emergence of spatial structure in cell groups and
583 the evolution of cooperation. *PLoS Comput. Biol.* **6**, e1000716 (2010).
584 19. Kim, H. J., Boedicker, J. Q., Choi, J. W. & Ismagilov, R. F. Defined spatial structure stabilizes
585 a synthetic multispecies bacterial community. *Proc. Natl. Acad. Sci.* **105**, 18188–18193
586 (2008).
587 20. Conrad, M. *et al.* Nutrient sensing and signaling in the yeast Saccharomyces cerevisiae. *FEMS*
588 *Microbiol. Rev.* **38**, 254–299 (2014).
589 21. Broach, J. R. Nutritional control of growth and development in yeast. *Genetics* **192**, 73–105
590 (2012).
591 22. Horák, J. Regulations of sugar transporters: insights from yeast. *Curr. Genet.* **59**, 1–31 (2013).
592 23. Watrous, J. *et al.* Mass spectral molecular networking of living microbial colonies. *Proc. Natl.*
593 *Acad. Sci. U. S. A.* **109**, E1743–E1752 (2012).
594 24. Traxler, M. F. & Kolter, R. A massively spectacular view of the chemical lives of microbes.
595 *Proc. Natl. Acad. Sci.* **109**, 10128–10129 (2012).
596 25. Bennett, M. R. & Hasty, J. Microfluidic devices for measuring gene network dynamics in
597 single cells. *Nat. Rev. Genet.* **10**, 628–638 (2009).
598 26. Cookson, S., Ostroff, N., Pang, W. L., Volfson, D. & Hasty, J. Monitoring dynamics of single-
599 cell gene expression over multiple cell cycles. *Mol. Syst. Biol.* **1**, E1–E6 (2005).
600 27. Robert, L. *et al.* Pre-dispositions and epigenetic inheritance in the Escherichia coli lactose
601 operon bistable switch. *Mol. Syst. Biol.* **6**, (2010).

602 28. Ni, M. *et al.* Pre-Disposition and Epigenetics Govern Variation in Bacterial Survival upon
603 Stress. *PLoS Genet.* **8**, (2012).
604 29. Llamosi, A. *et al.* What Population Reveals about Individual Cell Identity: Single-Cell
605 Parameter Estimation of Models of Gene Expression in Yeast. *PLOS Comput. Biol.* **12**,
606 e1004706 (2016).
607 30. Jo, M. C., Liu, W., Gu, L., Dang, W. & Qin, L. High-throughput analysis of yeast replicative
608 aging using a microfluidic system. *Proc. Natl. Acad. Sci.* **112**, 9364–9369 (2015).
609 31. Yang, Y. *et al.* Temporal scaling of ageing as an adaptive strategy of Escherichia coli. *bioRxiv*
610 376566 (2018). doi:10.1101/376566
611 32. Wang, P. *et al.* Robust growth of Escherichia coli. *Curr. Biol. CB* **20**, 1099–103 (2010).
612 33. Xu, Z. *et al.* Two routes to senescence revealed by real-time analysis of telomerase-negative
613 single lineages. *Nat. Commun.* **6**, 7680 (2015).
614 34. Lambert, G. & Kussel, E. Memory and Fitness Optimization of Bacteria under Fluctuating
615 Environments. *PLoS Genet.* **10**, (2014).
616 35. Prindle, A. *et al.* A sensing array of radically coupled genetic 'biopixels'. *Nature* **481**, 39–44
617 (2011).
618 36. Hornung Raphael *et al.* Quantitative modelling of nutrient-limited growth of bacterial colonies
619 in microfluidic cultivation. *J. R. Soc. Interface* **15**, 20170713 (2018).
620 37. Co, A. D., Vliet, S. van & Ackermann, M. Emergent microscale gradients give rise to
621 metabolic cross-feeding and antibiotic tolerance in clonal bacterial populations. *bioRxiv*
622 534149 (2019). doi:10.1101/534149
623 38. Wilmoth, J. L. *et al.* A Microfluidics and Agent-Based Modeling Framework for Investigating
624 Spatial Organization in Bacterial Colonies: The Case of Pseudomonas Aeruginosa and H1-
625 Type VI Secretion Interactions. *Front. Microbiol.* **9**, (2018).

626 39. Liu, J. *et al.* Metabolic co-dependence gives rise to collective oscillations within biofilms.
627 *Nature* **523**, 550–554 (2015).
628 40. Pfeiffer, T. & Morley, A. An evolutionary perspective on the Crabtree effect. *Front. Mol.*
629 *Biosci.* **1**, 17 (2014).
630 41. Hagman, A. & Piškur, J. A Study on the Fundamental Mechanism and the Evolutionary
631 Driving Forces behind Aerobic Fermentation in Yeast. *PLoS ONE* **10**, (2015).
632 42. Boyer, D. *et al.* Buckling instability in ordered bacterial colonies. *Phys. Biol.* **8**, 026008 (2011).
633 43. Reifenberger, E., Boles, E. & Ciriacy, M. Kinetic Characterization of Individual Hexose
634 Transporters of Saccharomyces Cerevisiae and their Relation to the Triggering Mechanisms
635 of Glucose Repression. *Eur. J. Biochem.* **245**, 324–333 (1997).
636 44. Diderich, J. A. *et al.* Glucose uptake kinetics and transcription of HXT genes in chemostat
637 cultures of Saccharomyces cerevisiae. *J. Biol. Chem.* **274**, 15350–9 (1999).
638 45. Maier, A., Völker, B., Boles, E. & Fuhrmann, G. F. Characterisation of glucose transport in
639 Saccharomyces cerevisiae with plasma membrane vesicles (countertransport) and intact cells
640 (initial uptake) with single Hxt1, Hxt2, Hxt3, Hxt4, Hxt6, Hxt7 or Gal2 transporters. *FEMS*
641 *Yeast Res.* **2**, 539–550 (2002).
642 46. Hovsepian, J. *et al.* Multilevel regulation of an α-arrestin by glucose depletion controls hexose
643 transporter endocytosis. *J Cell Biol* **216**, 1811–1831 (2017).
644 47. Verwaal, R. *et al.* HXT5 expression is determined by growth rates inSaccharomyces
645 cerevisiae. *Yeast* **19**, 1029–1038 (2002).
646 48. Otterstedt, K. *et al.* Switching the mode of metabolism in the yeast Saccharomyces cerevisiae.
647 *EMBO Rep.* **5**, 532–7 (2004).
648 49. Bonander, N. *et al.* Transcriptome analysis of a respiratory Saccharomyces cerevisiae strain
649 suggests the expression of its phenotype is glucose insensitive and predominantly controlled
650 by Hap4, Cat8 and Mig1. *BMC Genomics* **9**, 365 (2008).

651 50. Ohlmeier, S., Kastaniotis, A. J., Hiltunen, J. K. & Bergmann, U. The Yeast Mitochondrial
652 Proteome, a Study of Fermentative and Respiratory Growth. *J. Biol. Chem.* **279**, 3956–3979
653 (2004).
654 51. Granek, J. A. & Magwene, P. M. Environmental and Genetic Determinants of Colony
655 Morphology in Yeast. *PLOS Genet.* **6**, e1000823 (2010).
656 52. Flemming, H.-C. *et al.* Biofilms: an emergent form of bacterial life. *Nat. Rev. Microbiol.* **14**,
657 563–575 (2016).
658 53. Maršíková, J. *et al.* Metabolic differentiation of surface and invasive cells of yeast colony
659 biofilms revealed by gene expression profiling. *BMC Genomics* **18**, 814 (2017).
660 54. Palková, Z., Wilkinson, D. & Váchová, L. Aging and differentiation in yeast populations:
661 Elders with different properties and functions. *FEMS Yeast Res.* **14**, 96–108 (2014).
662 55. Campbell, K. *et al.* Self-establishing communities enable cooperative metabolite exchange in
663 a eukaryote. *eLife* **4**, 1–23 (2015).
664 56. Wintermute, E. H. & Silver, P. A. Dynamics in the mixed microbial concourse. *Genes Dev.*
665 **24**, 2603–2614 (2010).
666 57. Edelstein, A. D. *et al.* Advanced methods of microscope control using μManager software. *J.*
667 *Biol. Methods* **1**, e10 (2014).
668 58. Schneider, C. A., Rasband, W. S. & Eliceiri, K. W. NIH Image to ImageJ: 25 years of image
669 analysis. *Nat. Methods* **9**, 671–675 (2012).
670 59. Tinevez, J.-Y. *et al.* TrackMate: An open and extensible platform for single-particle tracking.
671 *Methods* **115**, 80–90 (2017).
672